



Influence of Microstructure and Defects on Mechanical Properties of AISI H13 Manufactured by Electron Beam Powder Bed Fusion

Moritz Kahlert , Florian Brenne, Malte Vollmer, and Thomas Niendorf

Submitted: 22 April 2021 / Revised: 17 June 2021 / Accepted: 10 July 2021 / Published online: 4 August 2021

Electron beam powder bed fusion (E-PBF) is a well-known additive manufacturing process. Components are realized based on layer-by-layer melting of metal powder. Due to the high degree of design freedom, additive manufacturing came into focus of tooling industry, especially for tools with sophisticated internal cooling channels. The present work focuses on the relationships between processing, microstructure evolution, chemical composition and mechanical properties of a high alloyed tool steel AISI H13 (1.2344, X40CrMoV5-1) processed by E-PBF. The specimens are free of cracks, however, lack of fusion defects are found upon use of non-optimized parameters finally affecting the mechanical properties detrimentally. Specimens built based on suitable parameters show a relatively fine grained bainitic/martensitic microstructure, finally resulting in a high ultimate strength and an even slightly higher failure strain compared to conventionally processed and heat treated AISI H13.

Keywords defects, electron beam melting (EBM), time-temperature-path, tool steel, mechanical properties

1. Introduction

Electron beam powder bed fusion (E-PBF), also known as Electron Beam Melting (EBM), is a powder bed-based layer-by-layer fabrication process being able to robustly produce metallic parts with a high density well above 99.5% showing mechanical properties similar to conventionally processed materials (Ref 1-3). It is well-known that microstructure evolution in E-PBF is highly influenced by the volume energy (Ref 1, 3). Usually powder layers with a thickness of about 50 μm are deposited in E-PBF. Afterward, the electron beam heats the powder bed in a pre-sintering process up to about 1000 $^{\circ}\text{C}$ and subsequently melts the powder locally. The high temperatures of the powder bed are realized by high-speed deflection of the electron beam. This process is repeated until the part is finished. Therefore, every layer is subjected to a cyclic heat treatment, which can influence the resulting properties (Ref 1). In recent years, the majority of studies on E-PBF focused on titanium- and nickel-based alloys, respectively, which are of significant interest for aerospace and

biomedical applications (Ref 1, 4). However, the process parameters necessary to obtain parts being characterized by low degrees of porosity are dependent on material specific parameters. Thus, process parameters have to be developed individually for each material. Since the process conditions and in particular the pre-sintering can prevent crack formation caused by internal stresses (Ref 5), E-PBF is promising for processing of materials, which are prone to crack formation. It has been revealed numerously that it is challenging to process brittle materials like, e.g., tool steels via laser powder bed fusion (L-PBF), since cracking and delamination often occur (Ref 6-9). Crack-free specimens of tool steels characterized by a relatively high density can be manufactured via L-PBF using baseplate heating and complex build strategies such as chessboard scanning pattern (Ref 6, 7, 10). Further studies also revealed the processability of a wide variety of tool steels such as AISI H11 (Ref 11-13), AISI H13 (Ref 7, 14-16), M2 (Ref 6, 17, 18) and Maraging 300 (Ref 19-21). However, the application of baseplate heating and complex build strategies clearly shows that extra efforts are needed to produce crack-free components out of many tool steels via L-PBF. Using E-PBF, Cormier et al. (Ref 22) demonstrated robust processability of AISI H13 tool steel being characterized by a fully martensitic microstructure upon processing using given process parameters. In addition, further studies reveal robust applicability of E-PBF especially for tool steels, rationalized by minor crack formation and low residual stresses resulting from less pronounced temperature gradients during cooling (Ref 22-24). However, to the best of the authors' knowledge, so far there are no studies available in open literature dealing with E-PBF processed AISI H13 providing for in-depth microstructural analysis and assessment of mechanical behavior. Moreover, results of recent studies investigating electron beam melting of AISI 4140 are limited in terms of their comparability, due to a different alloy composition resulting in different microstructures and mechanical properties (Ref 25, 26). Due to the above mentioned advantages, E-PBF is thought to be of great interest for processing of tool steels, especially since the geometrical

This invited article is part of a special topical focus in the *Journal of Materials Engineering and Performance* on Additive Manufacturing. The issue was organized by Dr. William Frazier, Pilgrim Consulting, LLC; Mr. Rick Russell, NASA; Dr. Yan Lu, NIST; Dr. Brandon D. Ribic, America Makes; and Caroline Vail, NSWC Carderock.

Moritz Kahlert, Florian Brenne, Malte Vollmer, and Thomas Niendorf, Institut für Werkstofftechnik (Materials Engineering), Universität Kassel, Mönchebergstraße 3, 34125 Kassel, Germany. Contact e-mail: kahlert@uni-kassel.de.

design freedom allows for integration of sophisticated functionality, e.g., conformal cooling (Ref 23, 24).

Although studies reporting on processing of tool steels via L-PBF gained increased attention in recent years, there is still a lack of literature reporting on processing of tool steels via E-PBF, especially AISI H13 as clearly stated by Balali et al. (Ref 27). In order to close this gap, the present study was conducted focusing on processing of AISI H13 via E-PBF without using Arcam AB auto functions. The resulting microstructures were analyzed by means of optical microscopy (OM), x-ray diffraction (XRD), scanning electron microscopy (SEM) and electron backscatter diffraction (EBSD) measurements. The chemical composition of the matrix and small precipitates were studied using energy dispersive x-ray spectroscopy (EDS). Finally, mechanical properties were investigated by hardness mappings and tensile tests. From results presented, process-microstructure-property relationships are drawn.

2. Materials and Methods

In the present study, an A2X E-PBF machine from Arcam AB was used. The machine has a maximum power of 3000 W and is able to heat the substrate plate up to temperatures of about 1000 °C. The build chamber comprises a controlled vacuum atmosphere including low partial pressure helium environment for increasing conductivity during processing. With respect to process parameter development for the AISI H13 tool steel, powders with a particle size range of 45 to 106 μm were used to build blocks with a size of 15 mm × 15 mm × 32 mm. The nominal chemical composition of the argon gas atomized powder (m4p material solutions GmbH, Germany) was 0.4% C, 5.3% Cr, 1.4% Mo, 1% V (wt %). A bidirectional scanning strategy with 90° rotation between the layers was applied. The nominal temperature of the substrate plate was 920 °C. The temperature was held for 30 min in order to sinter the powder under the substrate plate before the build process started. Parameters for pre-sintering and heating of the powder bed during processing are listed in Table 1.

The different parameters used for the melting process expand the standard parameter window Cormier et al. (Ref 22) used for their investigations and are shown in Table 2. The velocity, hatch distance and layer thickness were kept constant,

Table 1 Parameter set used for pre-sintering during manufacturing of AISI H13 via E-PBF

Power, W	Velocity, mm/s	Hatch distance, mm	Repetitions
1050	12000	1	25

Table 2 Parameter sets used for E-PBF processing in the present study

Parameter set	Power, W	Velocity, mm/s	Hatch distance, mm	Layer thickness, μm	Volume energy, J/mm ³
a	240	3000	0.05	50	32
b	270	3000	0.05	50	36
c	330	3000	0.05	50	44

whereas the power was changed. The chosen parameters result in three different volume energies (P_V), being listed in the last column. P_V is also referred to as volume energy density and energy density, respectively.

Tensile specimens based on ASTM E8 with geometrical dimensions shown in Fig. 1 were wire-cut by electrical discharge machining (EDM) from the 15 mm × 15 mm × 32 mm blocks. Before mechanical testing, the specimens were mechanically ground to 15 μm grit size, in order to avoid any influence of the EDM affected surface layers on the test results. In addition, specimens were sandblasted in the clamping area to ensure adequate contact conditions eventually avoiding slip within the grip section. The tensile tests were conducted using a 16 kN servohydraulic test rig at ambient conditions and constant crosshead displacement of 2 mm/min. Nominal strains were calculated based on displacement data. For each condition, at least three specimens were tested to evaluate repeatability.

For hardness measurements, specimens were polished down to a final grit size of 5 μm. A Struers - DuraScan 70 testing system was used, and a matrix of 4 × 50 indents (HV 5) was considered for mappings. The average hardness values were recalculated from all indents (HV 5) of a mapping.

For microstructural characterization, blocks were mechanically ground down to 5 μm grit size and subsequently vibropolished, using oxide polishing suspension for at least 12 h. A Zeiss Axio optical microscope (OM) was used for density analysis and evaluation of crack formation focusing on the polished specimens. For further microstructural characterization, a SEM Camscan MV3200 equipped with secondary electron (SE)-, back scattered electron (BSE)- and EDS-detectors was used. For EBSD measurements, a second SEM system (Zeiss Ultra) was used. Step size in case of the EBSD measurements was 0.1 μm. Both SEMs were operated at 20 kV. The fraction of retained austenite was experimentally determined by XRD using Mo-K α radiation and a collimator with a diameter of 2 mm. The investigated angle range (2θ) was 25° to 40° with a step size of 0.1° and a count time of 10 s. The 4-line method was used to evaluate the retained austenite content.

3. Results and Discussion

In order to evaluate the impact of the processing parameters on density, representative OM images of the specimens are shown in Fig. 2. In the specimen shown in a), being built with the lowest volume energy (32 J/mm³) considered in present work, flat horizontal pores can be seen, whereas the specimens shown in b) and c), built with higher volume energies (36 and 44 J/mm³, respectively) are characterized by superior relative

densities (porosity < 0.1 %). The OM images reveal that no crack formation occurred in any of the specimens studied irrespective of the energy volume density applied in E-PBF processing. The decrease in the relative density in case of the lowest volume energy considered here is most reasonably caused by lack of fusion defects, i.e., the energy input into the powder was too low to melt the powder layer to a sufficient depth (Ref 28).

Figure 3 reveals a needle-like microstructure for all conditions, indicating high amounts of martensite and bainite, respectively. However, in contrast to the L-PBF AISI H13 microstructure shown by Krell et al. (Ref 7), no cellular structures of retained austenite can be observed. Thus, the microstructure of E-PBF processed AISI H13 in this study is more similar to the microstructure of conventionally processed AISI H13. Additional XRD measurements focusing on retained austenite in the E-PBF processed AISI H13 specimens confirmed volume fractions below 5 % (not shown). It can be assumed that the long dwell time at relatively high temperatures leads to a homogeneous distribution of the alloying elements. Afterward, during relatively slow cooling (compared to the L-PBF process) a complete transformation occurs (a detailed

discussion about the cooling path is presented in the final paragraph of this chapter). The appearance of the needle-like structures, i.e., a slightly rounded shape, can be regarded as an indication of a bainitic structure. It is well-known that a clear distinction between both phases is difficult based on SEM micrographs only (Ref 29), however qualitative assessment is feasible. Discussion on microstructure evolution can be substantiated based on the well-known transformation behavior and paths, respectively, of conventionally processed AISI H13. This can be used as a basis to shed light on the potential phase distributions (cf. final paragraphs of this chapter and Fig. 8). From the BSE micrographs presented in Fig. 3, additional microstructural features can be distinguished.

A columnar superstructure (being hardly seen at the first glance) parallel to the build direction is highlighted in Fig. 3c. It is assumed that these structures are remaining traces of elongated prior austenitic grains occurring upon solidification and cooling. However, besides these traces, no further distinct anisotropic solidification structures (as known from austenitic stainless steels, e.g., AISI 316L (Ref 30)) are seen. The microstructure seems to primarily consist of the above mentioned very fine needle-like microstructure. Thus, phase transformations upon solidification and cooling are expected to have a dominant effect on the final microstructure appearance. This has been also revealed for other steels studied by some of the present authors as well, e.g., for AISI 4140 (Ref 25). Furthermore, Günther et al. (Ref 4) showed a fine grained microstructure in a metastable austenitic Cr-Mn-Ni steel manufactured by E-PBF. Grain refinement was attributed to a cyclic reheating of the single layers, i.e., intrinsic heat treatment being characteristic for E-PBF, leading to several solid-solid phase transformations. Eventually, it is expected that the intrinsic heat treatment leads to grain refinement in a similar fashion in case of the E-PBF processed AISI H13, however, being finally followed by a bainitic/martensitic transformation.

Fine distributed small white precipitates can be observed in all conditions (highlighted by white arrows in Fig. 3), and corresponding results obtained by chemical analysis are shown in Fig. 4. Comparing the peak intensities of the precipitates

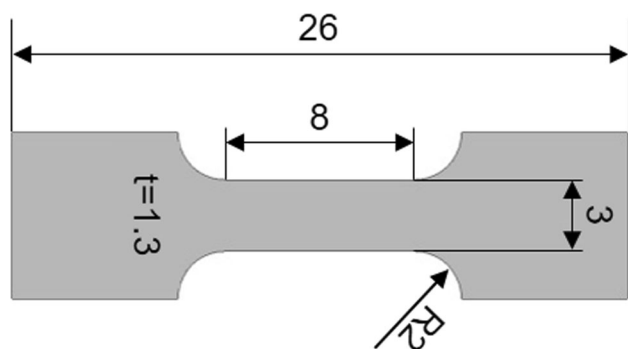


Fig. 1 Tensile specimen geometry employed for mechanical tests of AISI H13 processed via E-PBF. All dimensions are in mm

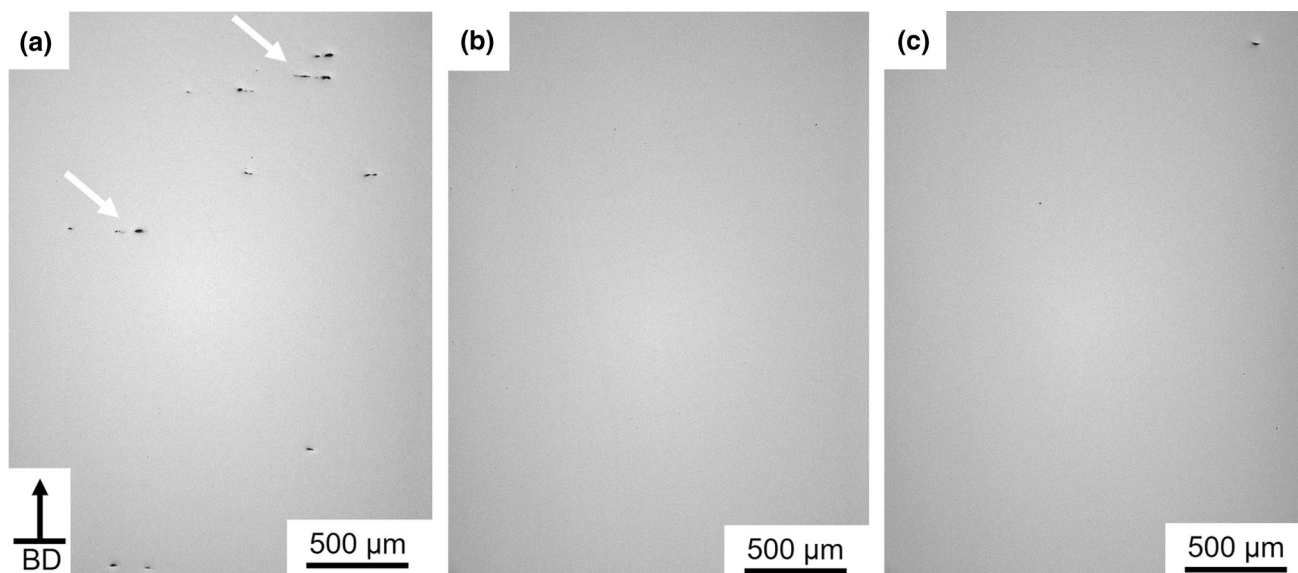


Fig. 2 Representative optical micrographs of AISI H13 E-PBF specimens built with different volume energies: (a) 32 J/mm³; (b) 36 J/mm³; (c) 44 J/mm³. Representative lack of fusion defects in a) are highlighted by white arrows

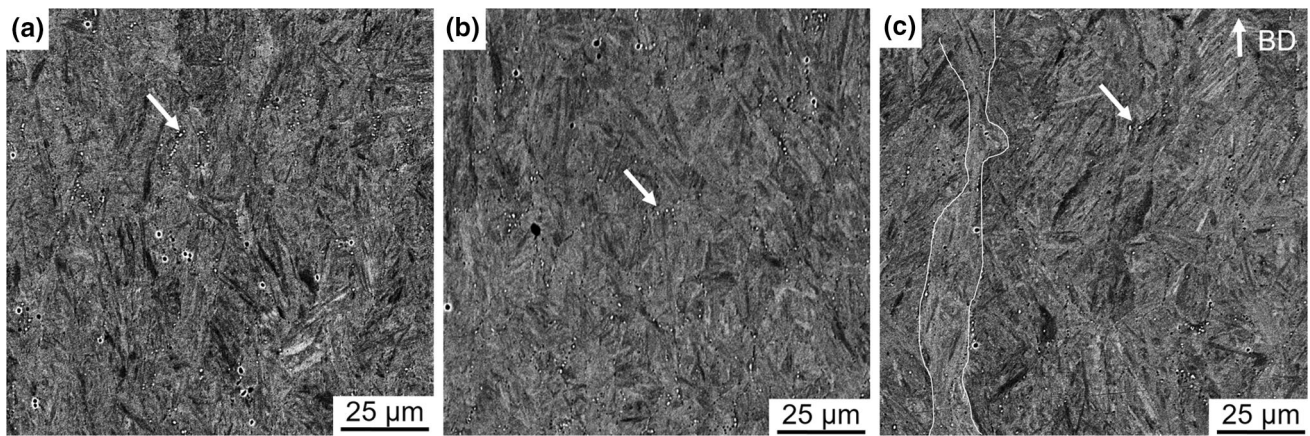


Fig. 3 BSE micrographs of AISI H13 processed via E-PBF with different volume energies: (a) 32 J/mm³; (b) 36 J/mm³; (c) 44 J/mm³

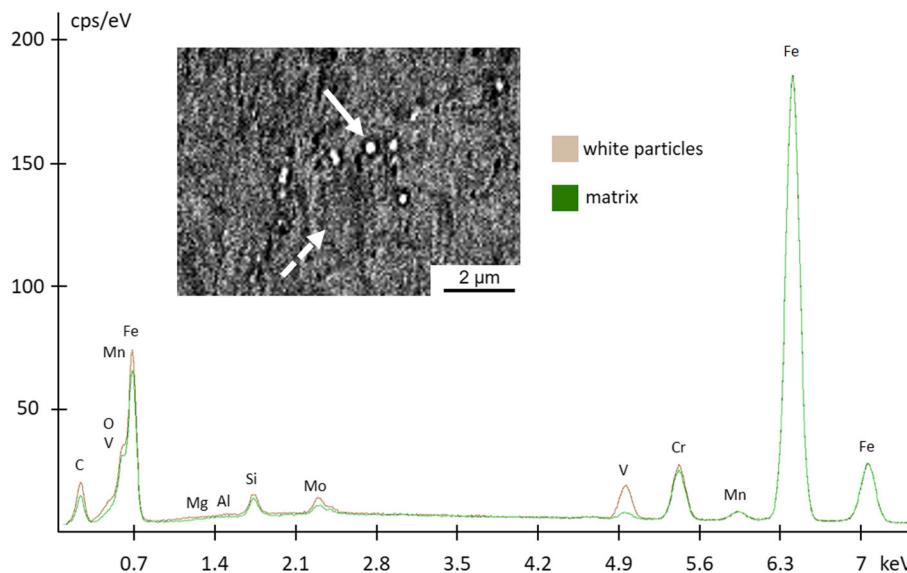


Fig. 4 EDS analysis qualitatively comparing the chemical composition of precipitates (highlighted by the white arrow in the inset) and the matrix (highlighted by the white dashed arrow in the inset) of E-PBF processed AISI H13

(brown) with the intensities of the matrix (green), higher intensities of the alloying elements vanadium and molybdenum can be seen. Especially, the peak intensity of vanadium in case of the precipitates is significantly higher than in case of the matrix. Since the formation of carbides is common for tool steels (Ref 31), it is likely that the precipitates seen are vanadium carbides. Cormier et al. (Ref 22) already revealed the presence of such families of precipitates for AISI H13 manufactured by E-PBF.

The EBSD IPF maps shown in Fig. 5 confirm the needle-like fine grained microstructure already highlighted by the BSE micrographs in Fig. 3. The needle-like structures are characterized by a distinct variant selection, i.e., preferred orientations of needles within a given volume (most probably a single prior austenitic grain), and hardly elongated in build direction. The mean dimensions of the needles virtually decrease with higher volume energies. The reason for this trend currently is not fully understood, however, it is likely that the grain refinement of prior austenite grains is affected by the intrinsic heat treatment as discussed above (Ref 4) eventually influencing the final

needle dimensions. Future studies will include high-resolution analysis of the nature of the needle-like structures seen to clearly separate bainite and martensite. Based on thorough analysis of such data, the elementary mechanisms contributing to a refinement of microstructure upon increase of energy density during E-PBF processing will then be revealed.

Figure 6 shows stress-strain diagrams of the different conditions obtained by tensile testing. For each condition, two curves are shown to assess repeatability of tests. The specimens built with the lowest volume energy density, show the lowest ultimate tensile strength and elongation at fracture. Such findings can be rationalized based on lack of fusion defects (Fig. 6b) and the overall low defect tolerance of the conditions considered. In contrast, specimens manufactured based on parameter sets leading to fully dense material (processing parameters being characterized by higher energy density) show a significant higher elongation at fracture. Specifically, specimens built with a volume energy of 44 J/mm³ show an elongation at fracture of about 13% in E-PBF as-built condition, which is significantly higher compared to

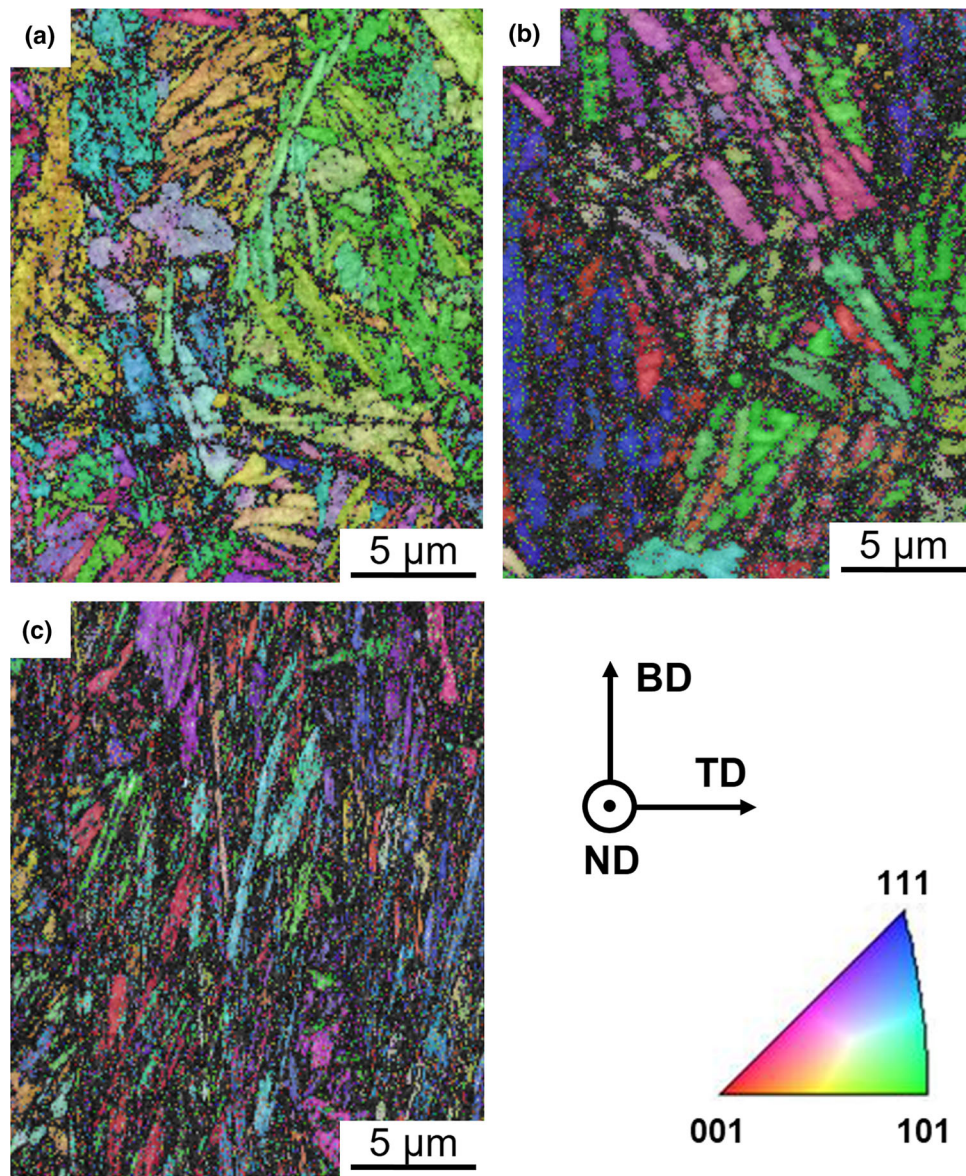


Fig. 5 EBSD inverse pole figure (IPF) maps of AISI H13 processed by E-PBF. The IPF maps are plotted for BD. Volume energies in E-PBF are: (a) 32 J/mm^3 ; (b) 36 J/mm^3 ; (c) 44 J/mm^3

values obtained from conventionally processed AISI H13 in heat treated condition (9% (Ref 32)).

Table 3 summarizes the mechanical properties obtained in the present study and provides mechanical properties of conventionally processed AISI H13 in a heat treated condition (Ref 32) for comparison. The hardness of the E-PBF processed specimens seems to slightly increase with higher volume energies, which is probably related to the finer needle structures shown before. The yield strength is only about 1100 MPa and, thus, much lower than the yield strength of the conventionally processed AISI H13 (1650 MPa (Ref 32)). The reason for the higher yield strength of the conventional AISI H13 is thought to be caused by the applied heat treatment of the conventional state resulting in a higher resistance against dislocation movement (Ref 29). However, the heat treatment is not described in detail in (Ref 32) and, thus, its implications are difficult to be discussed in-depth. Interestingly, pronounced hardening upon initial yielding is seen in the E-PBF

processed material, such that the difference in terms of ultimate tensile strength is reduced to only about 150 MPa at least for the two conditions built with relatively high energy densities. Due to the brittle behavior of the condition built with the lowest volume energy (32 J/mm^3), it shows inferior ultimate strength.

The fracture surface of an E-PBF AISI H13 specimen built with the lowest volume energy is shown in Fig. 7a. It is obvious from the highlighted area in Fig. 7d that some unmolten regions (with partially molten spherical particles attached) prevail on the fractured surface. The shape of the defects and the low volume energies used in this condition can be regarded as significant indicators for presence of lack of fusion defects. In contrast, no lack of fusion defects can be seen on the fracture surfaces of the conditions built with high volume energies (Fig. 7b-c and e-f). Moreover, the fracture surfaces of the specimens built with high volume energies are characterized by significant surface topography and a characteristic type of

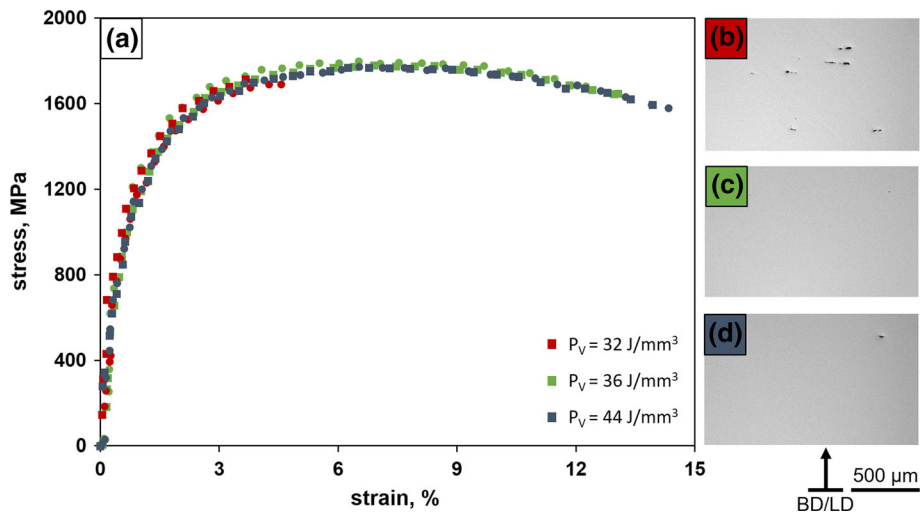


Fig. 6 (a) Stress-strain-diagrams of E-PBF AISI H13 specimens processed with different volume energies and (b-d) characteristic OM images revealing the related relative density of the conditions (cf. Fig. 2). For each condition, two representative curves are depicted

Table 3 Comparison of the results obtained by tensile tests for E-PBF processed and conventionally processed AISI H13 (Ref 32). For hardness values listed, the arithmetic mean value of the mappings shown in Fig. 9 was calculated

Parameter set	Volume energy, J/mm ³	Hardness, HV5	Yield strength, MPa	Ultimate strength, MPa	Elongation at fracture, %
a	32	507	1123	1715	3.2
b	36	513	1073	1796	11.7
c	44	519	1065	1772	13.2
conv.		...	1650	1990	9

fracture, respectively, indicating a relatively ductile material behavior.

The cooling rate is a key aspect for any kind of additive manufacturing technique. Especially for L-PBF it is well-known that without using a high-temperature baseplate heating, rapid cooling upon solidification is characterized by cooling rates up to 10^6 K/s (Ref 33) eventually leading to microstructures being far from equilibrium. In case of E-PBF processing, the course of cooling and, thus, evolution of microstructure is significantly different. To rationalize the reasons for this important difference in direct comparison of these two common powder bed techniques, the following considerations have to be taken into account: In case of L-PBF, general characteristics are somehow similar to E-PBF, i.e., the overall dimensions of the melt pool are small in comparison to the overall specimen dimensions. Thus, the heat from the melt pool can be rapidly transferred to the already solidified surrounding material after deflection of the beam, i.e., the energy source. Most important in terms of differences in case of the following thermal history, however, is the fact that E-PBF is a hot-bed process. Upon spreading of each individual powder layer, the powder bed is pre-heated by a defocused electron beam. This process step is crucially needed to avoid powder blasts, however, simultaneously changes the overall cooling path tremendously (when compared to L-PBF). The temperature of the baseplate shown in Fig. 8 is the best approximation of the real temperature of the specimen. After a pre-heating of the platform to 930 °C, the process is run at this temperature. To ensure that the

temperature in the uppermost layer remains on a relatively constant level, energy input during pre-heating is increased as a function of build height. Therefore, the temperature being measured at the fixed location below the initial build platform decreases even though the temperature in the build layer remains nearly constant. After finishing the build process, a short period of free cooling of the whole build and, thus, every single specimen, is enforced, followed by a more rapid cooling induced by helium (He) ventilation. In consequence, the cooling curve being responsible for the final microstructural appearance of the AISI H13 processed by E-PBF is not induced by a rapid quench from melting temperature down to a relatively low temperature level far below martensite start temperature (M_s). Instead, the E-PBF processed AISI H13 encounters rapid solidification, intrinsic heat treatment (i.e., thermal cycling), a long period of austenitization at a temperature level close to the pre-heating temperature, finally followed by slow cooling. The latter is only affected by the He-flow, which however is limited and, thus, far away from rapid quench conditions.

Figure 9 shows hardness mappings and line measurements being characteristic for the manufactured specimens along the build height. Clearly, the different volume energies do not significantly affect the general hardness distribution being characteristic for the AISI H13 specimens. It is rather obvious that the hardness values increase with the build height, i.e., the hardness in the base layers is about 500 HV and increases to about 580 HV in the top layers. It is likely that a slightly higher

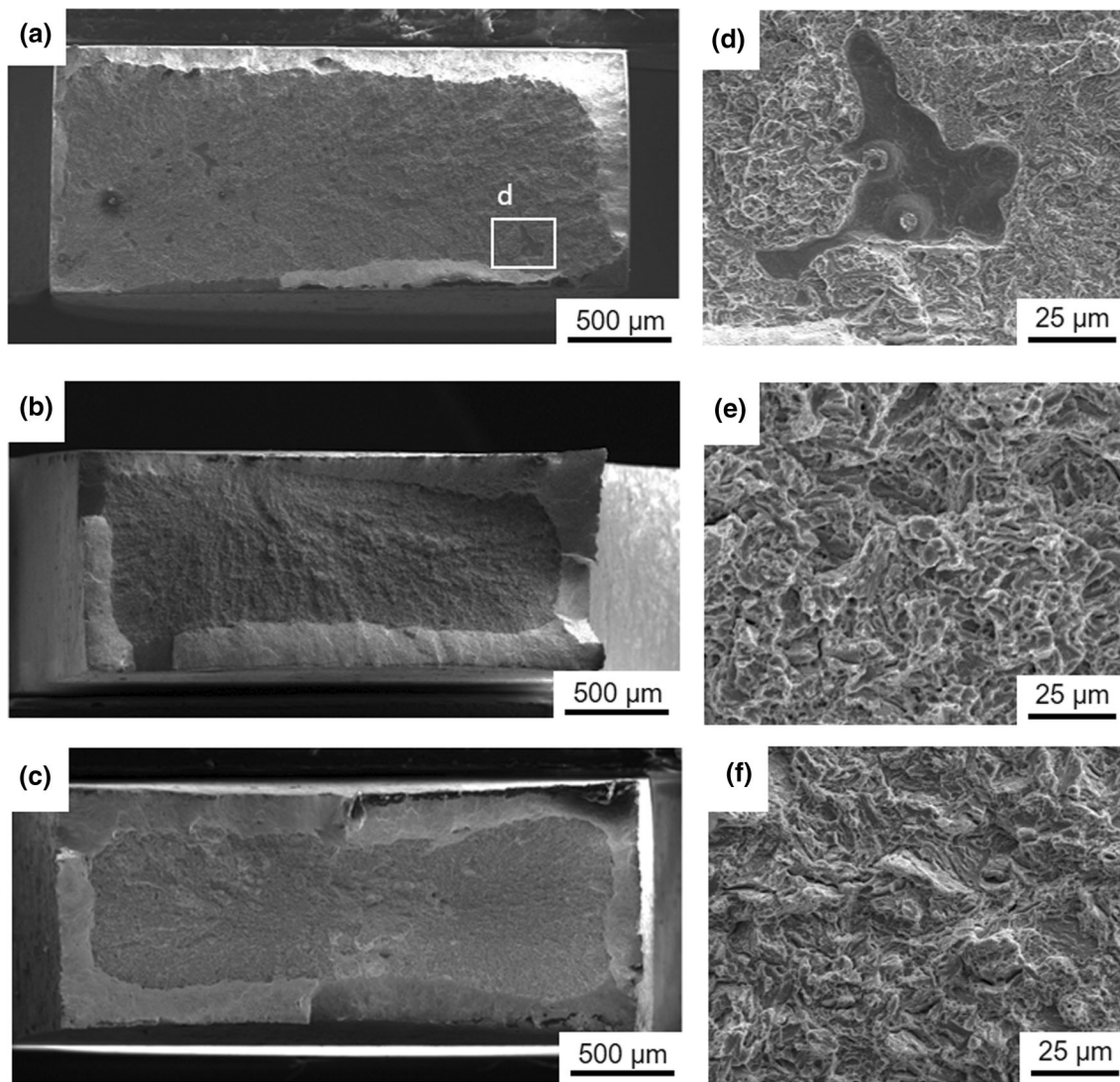


Fig. 7 SEM images detailing fracture surfaces upon tensile testing of AISI H13 specimens processed by E-PBF. Overview images being representative for conditions built with (a) 32 J/mm³; (b), 36 J/mm³; (c), 44 J/mm³; (d), (e), (f) insets highlighting the different morphologies of fracture surfaces

cooling rate of the top layers, being induced by the direct contact of the surfaces with the helium atmosphere (used to promote accelerated cooling of the whole build), results in a locally different fraction of bainite/martensite. Moreover, it is possible that deeper layers are subjected to annealing induced changes (e.g., coarsening of austenitic grains) during processing.

Continuous cooling transformation (CCT) phase diagrams are widely used to estimate the resulting microstructure and hardness of heat treated materials and steels, respectively. Unfortunately, such diagrams are not available for additively manufactured materials being characterized by unique microstructures as detailed before. Most important the complexity linked to intrinsic heat treatment is not considered in the CCT diagrams available so far. However, as already discussed in relation to Figure 8, the final microstructure appearance of the E-PBF AISI H13 is dominated by relatively slow cooling upon a long period of austenitization at the pre-heating temperature. Thus, estimation of microstructure evolution based on data available in literature is thought to be reasonable

at this point. A conventional CCT-diagram (Ref 34) was used to compare the experimentally determined hardness values of E-PBF AISI H13 in present work with values resulting from conventional heat treatments. Taking into account a cooling time of 120 min between 830 °C and 100 °C, as it is deduced from the base plate in the present study (Fig. 8), and, thus, a cooling rate of 6.1 °C/min, based on the CCT-diagram of AISI H13 (Ref 34) a hardness of roughly 550 HV is predicted, which is in good agreement with the results shown in Fig. 9. Thus, the final microstructure present in this condition (as directly deduced from the CCT-diagram) is estimated to be dominated by about 60 % of bainite. Although this results are in good agreement with the microstructural investigations shown before, it has to be noted that the considered CCT-diagram estimates phase evolution in AISI H13 upon austenitization at 1050 °C, whereas pre-heating temperature and, thus, maximum austenitization temperature for E-PBF AISI H13 was only 930 °C. Thus, in general an increased phase fraction of bainite is likely such that the absolute phase fraction in this

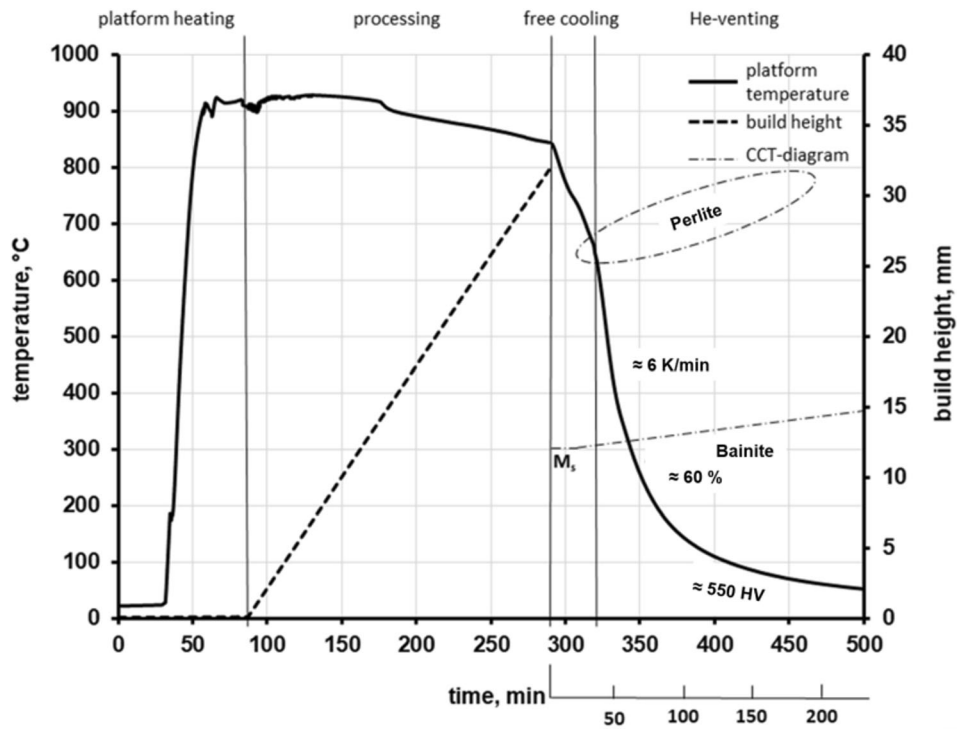


Fig. 8. The time-temperature path of the AISI H13 specimens processed via E-PBF. The cooling path is supplemented by a schematic CCT-diagram being recompiled from (Ref 34)

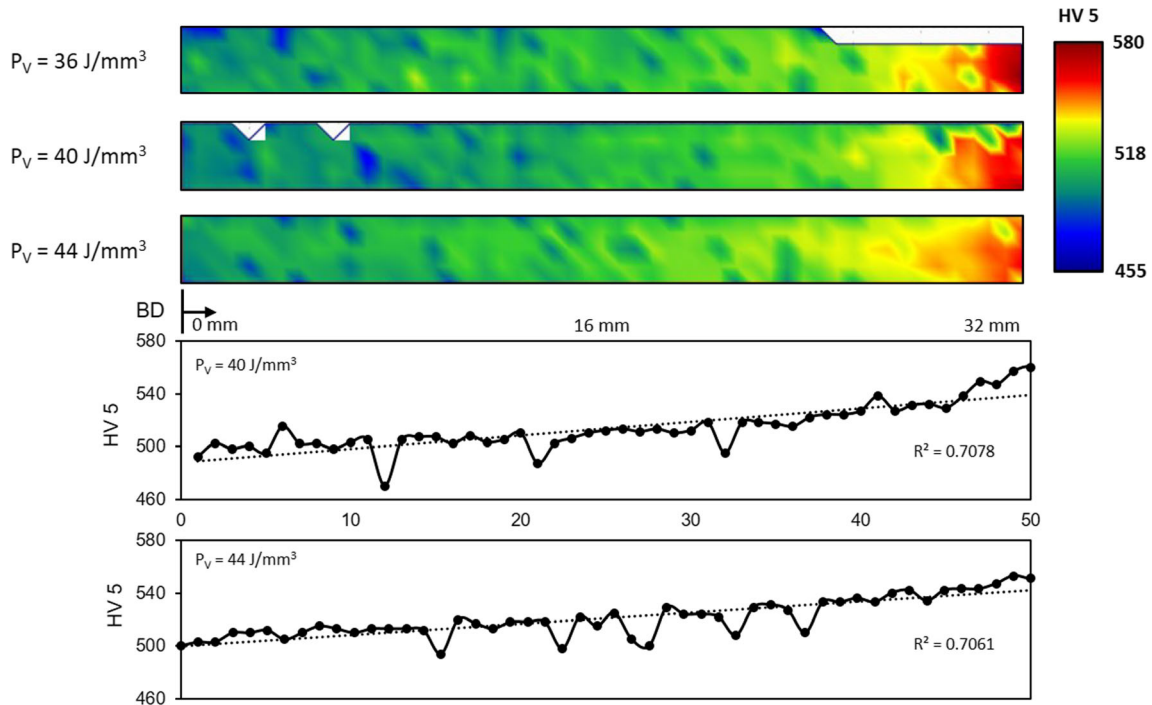


Fig. 9 Hardness mappings and hardness line measurements as a function of build height of AISI H13 specimens processed via E-PBF. The last molten layer is depicted on the right side of the figure, clearly being characterized by the highest hardness. The horizontal axis of the line measurement reveals the numbers of measuring points over the build height

study can differ from the prediction made based on the CCT-diagram.

4. Conclusions

In the present study, AISI H13 specimens were processed by electron beam powder bed fusion. It is shown that it is possible to obtain specimens with a high density and without any traces of process induced cracking. A fine grained needle-like microstructure and good mechanical properties are revealed. The main conclusions can be drawn as follows:

- (a) High relative densities without traces of large defects are found in all conditions built with high volume energies, i.e., 36 J/mm³ and 44 J/mm³, whereas the condition built with the lowest volume energy, i.e., 32 J/mm³, revealed a high density of lack of fusion defects. All conditions show a needle-like microstructure, which likely consist of a mixture of bainite and martensite, as well as small precipitates enriched in vanadium.
- (b) The mechanical properties, especially the elongation at fracture, are clearly influenced by the prevailing defect structures. The specimens being characterized by presence of lack of fusion defects show a significantly lower elongation at fracture as compared to specimens without lack of fusion defects. The specimens featuring high densities show very promising mechanical properties in E-PBF as-built condition, especially an ultimate strength very similar to conventionally processed and heat treated AISI H13.
- (c) Significant differences of hardness values have not been found for the differently processed E-PBF conditions, however, a distinct dependence of the hardness as a function of build height appeared. The highest hardness was found in the top layers. Thus, the hardness clearly is influenced by the time-temperature history, most importantly the cooling phase. In this regard, it has to be emphasized that cooling is relatively slow in the E-PBF process. This is due to the fact that E-PBF is a hot-bed process, where the whole part only cools down after final melting in the uppermost layer.

The results of the present study clearly reveal the high potential of manufacturing AISI H13 by E-PBF and, thus, open up a wide field of applications in industry, i.e., in the field of advanced casting molds enabled by conformal cooling. With respect to the envisaged industrial applications, the influence of the E-PBF process on the corrosion and fatigue properties, including thermal fatigue as well as thermo-shock loading, is of utmost importance and will be, thus, subject of future studies. Due to the ability of realizing unprecedented geometries and microstructures simultaneously, it is expected that parts of superior performance will be directly manufacturable by E-PBF.

Acknowledgments

The authors would like to thank voestalpine AG for supply of the powder material from m4p material solutions GmbH and Mr. Timo Thiel for supporting the experimental work.

Author Contributions

Conceptualization, M.K., F.B., M.V. and T.N.; methodology, F.B.; validation, M.K., M.V. and T.N.; investigation, F.B. and M.K.; resources, T.N.; data curation, M.K.; writing—original draft preparation, M.K.; writing—review and editing, M.V., M.K. and T.N.; visualization, M.K. and F.B.; supervision, M.V. and T.N.; project administration, T.N.; funding acquisition, T.N. All authors have read and agreed to the published version of the manuscript.

Funding

Open Access funding enabled and organized by Projekt DEAL. This research received no external funding.

Conflict of interest

The authors declare no conflict of interest.

Open Access

This article is licensed under a Creative Commons Attribution 4.0 International License, which permits use, sharing, adaptation, distribution and reproduction in any medium or format, as long as you give appropriate credit to the original author(s) and the source, provide a link to the Creative Commons licence, and indicate if changes were made. The images or other third party material in this article are included in the article's Creative Commons licence, unless indicated otherwise in a credit line to the material. If material is not included in the article's Creative Commons licence and your intended use is not permitted by statutory regulation or exceeds the permitted use, you will need to obtain permission directly from the copyright holder. To view a copy of this licence, visit <http://creativecommons.org/licenses/by/4.0/>.

References

1. M. Galati and L. Luliano, A Literature Review of Powder-Based Electron Beam Melting Focusing on Numerical Simulations, *Addit. Manuf.*, 2018, **19**, p 1–20
2. L.-C. Zhang, Y. Liu, S. Li and Y. Hao, Additive Manufacturing of Titanium Alloys by Electron Beam Melting: A Review, *Adv. Eng. Mater.*, 2018, **20**(5), art no 1700842
3. C. Körner, Additive Manufacturing of Metallic Components by Selective Electron Beam Melting — A Review, *Int. Mater. Rev.*, 2016, **61**(5), p 361–377
4. J. Günther, F. Brenne, M. Droste, M. Wendler, O. Volkova, H. Biermann and T. Niendorf, Design of Novel Materials for Additive Manufacturing - Isotropic Microstructure and High Defect Tolerance, *Sci. Rep.*, 2018, **8**(1), art no 1298
5. L.M. Sochalski-Kolbus, E.A. Payzant, P.A. Cornwell, T.R. Watkins, S.S. Babu, R.R. Dehoff, M. Lorenz, O. Ovchinnikova and C. Duty, Comparison of Residual Stresses in Inconel 718 Simple Parts Made by Electron Beam Melting and Direct Laser Metal Sintering, *Metall and Mat Trans A*, 2015, **46**(3), p 1419–1432
6. K. Kempen, B. Vrancken, S. Buls, L. Thijs, J. van Humbeeck and J.-P. Kruth, Selective Laser Melting of Crack-Free High Density M2 High Speed Steel Parts by Baseplate Preheating, *J. Manuf. Sci. Eng.*, 2014, **136**(6), art no 61026
7. J. Krell, A. Roettger, K. Geenen and W. Theisen, General Investigations on Processing Tool Steel X40CrMoV5-1 with Selective Laser Melting, *J. Mater. Process. Technol.*, 2018, **255**, p 679–688
8. M. Yonehara, T.-T. Ikeshoji, T. Nagahama, T. Mizoguchi, M. Tano, T. Yoshimi and H. Kyogoku, Parameter Optimization of the High-Power Laser Powder Bed Fusion Process for H13 Tool Steel, *Int J Adv Manuf Technol*, 2020, **110**(1–2), p 427–437

9. L. Wu, S. Das, W. Gridin, S. Leuders, M. Kahlert, M. Vollmer and T. Niendorf, Hot Work Tool Steel Processed by Laser Powder Bed Fusion: A Review on Most Relevant Influencing Factors, *Adv. Eng. Mater.*, 2021, **63**, art no 2100049
10. J. Sander, J. Hufenbach, L. Giebeler, H. Wendrock, U. Kühn and J. Eckert, Microstructure and Properties of FeCrMoVC Tool Steel Produced by Selective Laser Melting, *Mater. Des.*, 2016, **89**, p 335–341
11. A. Armillotta, R. Baraggi and S. Fasoli, SLM Tooling for Die Casting with Conformal Cooling Channels, *Int J Adv Manuf Technol*, 2014, **71**(1–4), p 573–583
12. R. Casati, M. Coduri, N. Lecis, C. Andrianopoli and M. Vedani, Microstructure and Mechanical Behavior of Hot-Work Tool Steels Processed by Selective Laser Melting, *Mater. Charact.*, 2018, **137**, p 50–57
13. F. Huber, C. Bischof, O. Hentschel, J. Heberle, J. Zettl, K.Y. Nagulin and M. Schmidt, Laser beam melting and heat-treatment of 1.2343 (AISI H11) tool steel – microstructure and mechanical properties, *Mater. Sci. Eng. A*, 2019, **742**, p 109–115
14. C.S. Wright, M. Youseffi, S.P. Akhtar, T.H.C. Childs, C. Hauser and P. Fox, Selective Laser Melting of Prealloyed High Alloy Steel Powder Beds, *MSF*, 2006, **514–516**, p 516–523
15. B. Breidenstein, F. Brenne, L. Wu, T. Niendorf and B. Denkena, Effect of Post-Process Machining on Surface Properties of Additively Manufactured H13 Tool Steel, *HTM, J. Heat Treat. Mater.*, 2018, **73**(4), p 173–186
16. E. Guenther, M. Kahlert, M. Vollmer, T. Niendorf and C. Greiner, Tribological Performance of Additively Manufactured AISI H13 Steel in Different Surface Conditions, *Materials*, 2021, **14**(4), art no 928
17. Z.H. Liu, D.Q. Zhang, C.K. Chua and K.F. Leong, Crystal Structure Analysis of M2 High Speed Steel Parts Produced by Selective Laser Melting, *Mater. Charact.*, 2013, **84**, p 72–80
18. M. Zhang, C. Chen, L. Qin, K. Yan, G. Cheng, H. Jing and T. Zou, Laser Additive Manufacturing of M2 High-Speed Steel, *Mater. Sci. Technol.*, 2018, **34**(1), p 69–78
19. E.A. Jäggle, P.-P. Choi, J. van Humbeeck and D. Raabe, Precipitation and Austenite Reversion Behavior of a Maraging Steel Produced by Selective Laser Melting, *J. Mater. Res.*, 2014, **29**(17), p 2072–2079
20. Y. Bai, Y. Yang, Di Wang and M. Zhang, Influence Mechanism of Parameters Process and Mechanical Properties Evolution Mechanism of Maraging Steel 300 by Selective Laser Melting, *Mater. Sci. Eng. A*, 2017, **703**(2), p 116–123
21. E.A. Jäggle, Z. Sheng, P. Kürmsteiner, S. Ocylok, A. Weisheit and D. Raabe, Comparison of Maraging Steel Micro- and Nanostructure Produced Conventionally and by Laser Additive Manufacturing, *Materials*, 2016, **10**(1), art no 8
22. D. Cormier, A. Harrysson and H. West, Characterization of H13 Steel Produced Via Electron Beam Melting, *Rapid Prototyping J.*, 2004, **10**(1), p 35–41
23. L.-E. Rännar, A. Glad and C.-G. Gustafson, Efficient Cooling with Tool Inserts Manufactured by Electron Beam Melting, *Rapid Prototyping J.*, 2007, **13**(3), p 128–135
24. G.J. Gibbons and R.G. Hansell, Direct Tool Steel Injection Mould Inserts through the Arcam EBM free-form Fabrication Process, *Assem. Autom.*, 2005, **25**(4), p 300–305
25. A. Fischer, M. Vollmer, P. Krooß and T. Niendorf, Microstructural and Mechanical Properties of AISI 4140 Steel Processed by Electron Beam Powder Bed Fusion Analyzed using Miniature Samples, Selected Technical Papers 1637, 2021, accepted for publication
26. M. Jurisch, B. Klöden, A. Kirchner, G. Walther and T. Weißgärber, SEBM Processing of 42CrMo4, *Prog Addit Manuf*, 2020, **5**(1), p 27–32
27. P. Bajaj, A. Hariharan, A. Kini, P. Kürmsteiner, D. Raabe and E.A. Jäggle, Steels in Additive Manufacturing: A Review of their Microstructure and Properties, *Mater. Sci. Eng. A*, 2020, **772**, art no 138633
28. Q.C. Liu, J. Elambasseril, S.J. Sun, M. Leary, M. Brandt and P.K. Sharp, The Effect of Manufacturing Defects on the Fatigue Behaviour of Ti-6Al-4V Specimens Fabricated Using Selective Laser Melting, *Adv. Mater. Res.*, 2014, **891–892**, p 1519–1524
29. H.-J. Bargel and G. Schulze, *Werkstoffkunde (Materials Science)*, 11th ed. Springer, Berlin, Heidelberg, 2012. **(in German)**
30. Y. Zhong, L.-E. Rännar, L. Liu, A. Koptyug, S. Wikman, J. Olsen, D. Cui and Z. Shen, Additive Manufacturing of 316L Stainless Steel by Electron Beam Melting for Nuclear Fusion Applications, *J. Nucl. Mater.*, 2017, **486**, p 234–245
31. G.A. Roberts, G. Krauss and R. Kennedy, *Tool Steels*, 5th ed. The Materials Information Society, Materials Park, Ohio, ASM International, 1998
32. R. Mertens, B. Vrancken, N. Holmstock, Y. Kinds, J.-P. Kruth and J. van Humbeeck, Influence of Powder Bed Preheating on Microstructure and Mechanical Properties of H13 Tool Steel SLM Parts, *Phys. Procedia*, 2016, **83**, p 882–890
33. H.K. Rafi, N.V. Karthik, H. Gong, T.L. Starr and B.E. Stucker, Microstructures and Mechanical Properties of Ti6Al4V Parts Fabricated by Selective Laser Melting and Electron Beam Melting, *J. of Mater. Eng and Perform.*, 2013, **22**(12), p 3872–3883
34. Kind & Co Edelmetallwerk, Datasheet Dominial USD 1.2344, http://www.kindtakimcelik.com/de/_download/warmarbeitskatalog.pdf. Accessed 31 May 2021

Publisher's Note Springer Nature remains neutral with regard to jurisdictional claims in published maps and institutional affiliations.